NASA Technical Memorandum 101488
ICOMP-89-5

Control-Volume Based Navier-Stokes Equation Solver Valid at All Flow Velocities

S.-W. Kim
Institute for Computational Mechanics in Propulsion
Lewis Research Center
Cleveland, Ohio

February 1989

NASA

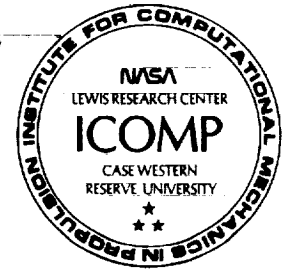

CONTROL-VOLUME BASED NAVIER-STOKES EQUATION SOLVER VALID AT ALL FLOW VELOCITIES

S.-W. Kim*
Institute for Computational Mechanics in Propulsion
Lewis Research Center
Cleveland, Ohio 44135

SUMMARY

A control-volume based finite difference method to solve the Reynolds averaged Navier-stokes equations is presented. A pressure correction equation valid at all flow velocities and a pressure staggered grid layout are used in the method. Example problems presented herein include: a developing laminar channel flow, a developing laminar pipe flow, a lid-driven square cavity flow, a laminar flow through a 90-degree bent channel, a laminar polar cavity flow, and a turbulent supersonic flow over a compression ramp. A k-ϵ turbulence model supplemented with a near-wall turbulence model was used to solve the turbulent flow. It is shown that the method yields accurate computational results even when highly skewed, unequally spaced, curved grids are used. It is also shown that the method is strongly convergent for high Reynolds number flows.

*Work funded under Space Act Agreement C99066G.

Nomenclature

A_u	coefficient for incremental u-velocity
A_v	coefficient for incremental v-velocity
A_1	constant coefficient for f_μ equation (=0.025)
A_2	constant coefficient for f_μ equation (=0.00001)
A_ϵ	constant coefficient for f_ϵ equation
c_ℓ	turbulence model constants for ϵ equation, (ℓ=1,2)
$c_{\mu f}$	constant coefficient for eddy viscosity equation (=0.09)
d_n	normal distance from wall
f_μ	wall damping function for eddy viscosity equation
f_ϵ	wall damping function for ϵ_w equation
k	turbulent kinetic energy
k_e	effective thermal conductivity ($=k_m+k_t$)
k_m	thermal conductivity
k_t	turbulent thermal conductivity ($=C_p\mu_t/\sigma_T$)
n	outward normal vector, ($=\{n_x, n_y\}$)
p	pressure
P_r	production rate of turbulent kinetic energy
R	gas constant.
Re	Reynolds number
R_t	turbulent Reynolds number ($=k^2/(\nu\epsilon_1)$)
T	temperature
u_τ	friction velocity ($=\sqrt{(\tau_w/\rho)}$)
V	velocity vector ($=\{u,v\}$)
x	cartesian coordinates ($=\{x,y\}$)
y^+	wall coordinate ($=u_\tau d_n/\nu$)
ϵ	dissipation rate

ϵ_l	dissipation rate of turbulent kinetic energy
ϵ_w	dissipation rate inside the near-wall layer
κ	von Karman constant (=0.41)
μ	molecular viscosity
μ_e	effective viscosity ($=\mu+\mu_t$)
μ_t	turbulent viscosity
ν	kinematic viscosity of fluid
ν_t	turbulent eddy viscosity
(ξ,η)	curvilinear coordinates
ρ	density
σ_k	turbulent Prandtl number for k-equation
σ_T	turbulent Prandtl number for energy equation
σ_ϵ	turbulent Prandtl number for ϵ-equation
τ_w	wall shearing stress
Φ	dissipation function for energy equation

Superscripts

^	non-dimensional value normalized by the free stream value
n	iteration level
*	current value
'	incremental (or corrective) value

Subscripts

nb	neighboring grid points, (=(E, W, S, N))
P	grid point

Mathematical symbol

$\sum$	summation

INTRODUCTION

A control-volume based finite difference method to solve the Reynolds averaged Navier-Stokes equations for all flow velocities is presented. The method is an extension of the pressure correction method (SIMPLE) which is used primarily to solve incompressible flows [1,2]. Numerical methods based on the pressure correction method have been used extensively to solve complex turbulent flows [3], including chemically reacting turbulent flows [4], due to their strongly convergent nature. In the present study, a pressure correction equation which is valid at all flow velocities is used for numerical calculations of incompressible and compressible flows.

Many finite difference methods to solve the compressible flow equations are based on the flux-splitting method. The Beam-Warming method [5] and the McCormack method [6] are the representatives of the flux-splitting methods. The flux-splitting methods were originally developed to solve the Euler equations and then extended to include the viscous term to solve the Navier-Stokes equations. The most distinguishing practical difference between the pressure correction methods and the flux-splitting methods lies in the way the diffusion term is treated. In the former class of methods, the diffusion term has been incorporated into the stiffness matrix while, in the latter class of methods, the diffusion term has been incorporated into the system of equations as the load vector term. For turbulent flows with extensive recirculation zones, the pressure correction methods may be numerically more stable conceptually. However, the pressure correction methods have mostly been used for incompressible flows and the flux splitting methods have mostly been used for compressible flows. Therefore, definitive advantages and disadvantages of these two classes of methods can not be discussed with confidence as yet.

The original numerical method based on the SIMPLE algorithm [2] is used to solve the Navier-Stokes equations whose domain can be discretized using orthogonal grids. A fully staggered grid layout [1] has been used in the method. However, in many flow problems of practical importance, the boundary geometries are complex and arbitrary shaped blockages may exist inside the flow path. A number of papers to extend the pressure correction methods for flows with arbitrary geometries and for compressible flows have appeared in recent years [7-13].

A number of grid layouts have been proposed and tested to identify the most suitable one to solve the Navier-Stokes equations defined on arbitrary, complex geometries. In Reference 7, the standard fully staggered grid layout, Figure 1-(a), was used to solve the Navier-Stokes equations defined on curved geometries. This grid layout can not be used to solve flows inside 90-degree bent ducts (see Reference 8 for details). A collocated grid layout, Figure 1-(b), was used in References 9 and 10. In Reference 9, the velocity - pressure decoupling was prevented by including an artificial viscosity, while in Reference 10, the same purpose was achieved by evaluating the incremental velocities at mid-sides of the control volume. In Reference 8, the standard fully staggered grid was used and the velocity vector was located at all grid points except at the pressure grid point (see Figure 1-(c)). In this case, the number of degrees of freedom for velocity is doubled while that of pressure remains the same as in the original case. Note that the accuracy of numerical solutions depends not only on the number of velocity grid points but also on the number of pressure grid points. Hence the accuracy can not be improved as much as the doubled number of velocity grid points might suggest. In References 12 and 13, the velocities were located at the same grid points

and the pressure was located at the centroid of the cell formed by the four adjacent velocity grid points (see Figure 1-(d)). This grid layout has been used successfully in penalty finite element methods for a long time [14]. It was first used in the control-volume based finite difference method in Vanka et. al. [12]. They mentioned that it was not easy to obtain convergent solutions due to the velocity-pressure decoupling. The mechanism that yields the velocity-pressure decoupled solution was heuristically shown in Reference [8]. In Reference 13, the velocity-pressure decoupling was eliminated by using a non-conforming domain for the mass imbalance calculation. In the present study, the velocity-pressure decoupling was eliminated by moving the off-diagonal terms to the load vector term. The resulting system of equations was solved using the Tri-Diagonal Matrix Algorithm (TDMA) [1]. Thus any uncertainty that may arise due to the use of a non-conforming domain for the mass imbalance calculation does not exist in the present method.

A few different numerical procedures have also been used to solve the pressure correction equation for compressible flows. The SIMPLE-R [1] and the SIMPLE-C [15] were used in References 11 and 13, respectively. The pressure, velocity, and density were corrected based on the incremental pressure (or pressure correction) in References 11 and 13. In the present study, only the pressure and velocity were corrected from the incremental pressure as in the standard SIMPLE method [1]. Density was obtained from the equation of state for perfect gas so that the same numerical procedure could equally be applicable for numerical computations of chemically reacting turbulent flows in the future. The numerical procedure to solve the pressure correction equation for compressible flows may need to be studied further in the future.

A k-ϵ turbulence model supplemented with a near-wall turbulence model was used in the present study. Establishment of the near-wall turbulence model and its application to fully developed turbulent channel and pipe flows can be found in Reference 16. It has been shown in the reference that the near-wall turbulence model can resolve the over-shoot phenomena of the turbulent kinetic energy and the dissipation rate in the region very close to the wall. Thus significantly improved computational results for the near-wall turbulence structure were obtained. It is also shown in Reference 17 that the turbulence model yields correct location of the shock for a transonic flow over an axisymmetric curved hill with shock wave - turbulent boundary layer interaction [18].

A number of flow cases have been solved to test the accuracy and the convergence nature of the present numerical method. The example flows presented herein include: a developing laminar channel flow, a developing laminar pipe flow, a lid-driven square cavity flow [19-21], a two-dimensional laminar flow in a 90-degree bent channel, a polar cavity flow [22], and a turbulent supersonic flow over a compression ramp [23-24].

REYNOLDS AVERAGED NAVIER-STOKES EQUATIONS FOR COMPRESSIBLE FLOWS

The compressible turbulent flow equations are given as;

$$\frac{\partial}{\partial x}(\rho u) + \frac{\partial}{\partial y}(\rho v) = 0. \tag{1}$$

$$\frac{\partial}{\partial x}(\rho uu) + \frac{\partial}{\partial y}(\rho vu) = \frac{\partial}{\partial x}(\tau_{xx}) + \frac{\partial}{\partial y}(\tau_{xy}) - \frac{\partial p}{\partial x} \tag{2}$$

$$\frac{\partial}{\partial x}(\rho uv) + \frac{\partial}{\partial y}(\rho vv) = \frac{\partial}{\partial x}(\tau_{yx}) + \frac{\partial}{\partial y}(\tau_{yy}) - \frac{\partial p}{\partial y} \tag{3}$$

$$\frac{\partial}{\partial x}(\rho C_p uT) + \frac{\partial}{\partial y}(\rho C_p vT) = \frac{\partial}{\partial x}\left[k_e \frac{\partial T}{\partial x}\right] + \frac{\partial}{\partial y}\left[k_e \frac{\partial T}{\partial y}\right] + u\frac{\partial p}{\partial x} + v\frac{\partial p}{\partial y} + \Phi \tag{4}$$

where

$$\tau_{xx} = 2\mu_e \frac{\partial u}{\partial x} - \frac{2\mu_e}{3}(\nabla \cdot \mathbf{V}),$$

$$\tau_{xy} = \tau_{yx} = \mu_e\left[\frac{\partial u}{\partial y} + \frac{\partial v}{\partial x}\right],$$

$$\tau_{yy} = 2\mu_e \frac{\partial v}{\partial y} - \frac{2\mu_e}{3}(\nabla \cdot \mathbf{V}),$$

$$\Phi = \mu_e \left\{ 2\left[\frac{\partial u}{\partial x}\right]^2 + 2\left[\frac{\partial v}{\partial y}\right]^2 + \left[\frac{\partial u}{\partial y} + \frac{\partial v}{\partial x}\right]^2 \right\} - \frac{2\mu_e}{3}(\nabla \cdot \mathbf{V})^2,$$

$$\nabla \cdot \mathbf{V} = \frac{\partial u}{\partial x} + \frac{\partial v}{\partial y},$$

and the density is obtained from the perfect gas law given as $p=\rho RT$. The turbulent Prandtl number (σ_T) of 0.75 was used for the energy equation in the present calculations. The compressible turbulent flow equations for axisymmetric case can be found in Reference 17.

The molecular viscosity and the thermal conductivity were obtained

from the Sutherland's laws given as [25];

$$\frac{\mu}{\mu_o} = \left(\frac{T}{T_o}\right)^{3/2} \left(\frac{T_o + S}{T + S}\right) \tag{5}$$

where $\mu_o = 1.716 \times 10^{-5}$ Kg/m-sec, $T_o = 273.1^o$ K, $S = 110.6^o$ K; and

$$\frac{k_m}{k_o} = \left(\frac{T}{T_o}\right)^{3/2} \left(\frac{T_o + S}{T + S}\right) \tag{6}$$

where $k_o = 0.0264$ Kg/m-K, $T_o = 273.1^o$ K, and $S = 194.4^o$ K.

TURBULENCE EQUATIONS

A k-ϵ turbulence model supplemented with a near-wall turbulence model is described below [16,17]. The turbulent kinetic energy equation for the entire flow domain is given as;

$$\frac{\partial}{\partial x}(\rho uk) + \frac{\partial}{\partial y}(\rho vk) = \frac{\partial}{\partial x}\left[\mu_e \frac{\partial k}{\partial x}\right] + \frac{\partial}{\partial y}\left[\mu_e \frac{\partial k}{\partial y}\right] + \rho Pr - \rho\epsilon \tag{7}$$

where the production rate of turbulent kinetic energy (Pr) is the same as the dissipation function for the energy equation (Φ).

The dissipation rate inside the near-wall layer is given as;

$$\epsilon_w = \frac{\epsilon_1}{f_\epsilon} \tag{8}$$

where

$$\left.\begin{aligned} \epsilon_1 &= \frac{c_{\mu f}{}^{3/4} k^{3/2}}{\kappa d_n} \\ f_\epsilon &= 1 - \exp(-A_\epsilon R_t) \\ R_t &= \frac{k^2}{\nu \epsilon_1} \\ A_\epsilon &= \frac{c_{\mu f}{}^{3/2}}{2\kappa^2} \end{aligned}\right\} \qquad (9)$$

The dissipation rate given as eq. (8) is used for eq. (7) in the near-wall region. The dissipation rate for the rest of the flow domain is obtained by solving the convection-diffusion equation for the dissipation rate equation given as;

$$\frac{\partial}{\partial x}(\rho u \epsilon) + \frac{\partial}{\partial y}(\rho v \epsilon) = \frac{\partial}{\partial x}\left[\mu_e \frac{\partial \epsilon}{\partial x}\right] + \frac{\partial}{\partial y}\left[\mu_e \frac{\partial \epsilon}{\partial y}\right] + \rho c_1 \frac{Pr\epsilon}{k} - \rho c_2 \frac{\epsilon^2}{k} \qquad (10)$$

The turbulence model constants used are given as: σ_k=0.75, σ_ϵ=1.15, c_1=1.39, and c_2=1.88. These turbulence model constants approximately satisfy the near-wall equilibrium turbulence condition and an experimentally observed decay rate of the grid turbulence [26]. Further discussion on the establishment of these constants can be found in References 27-28.

The eddy viscosity inside the near-wall layer is given as;

$$\nu_t = c_{\mu f} f_\mu \frac{k^2}{\epsilon_1} \tag{11}$$

where f_μ=1-exp($A_1/R_t + A_2 R_t^2$) . The wall damping function f_μ is a linear function of the distance from the wall in the viscous sublayer and becomes unity in the fully turbulent region. The eddy viscosity, given as eq. (11), grows in proportion to the cubic power of the distance from the wall. The eddy viscosity in the rest of the flow domain is given as;

$$\nu_t = c_{\mu f} \frac{k^2}{\epsilon} \tag{12}$$

The partition between the near-wall region and the fully turbulent outer region can be located between y^+ greater than 100 and less than 300 approximately. Details on the k-ϵ turbulence model supplemented with the near-wall turbulence model can be found in References 16 and 17.

NUMERICAL METHOD

In the present method, all flow variables, except pressure, have been located at the same grid points and the pressure node has been located at the centroid of the cell formed by the four neighboring velocity grid points. Note that in the control-volume methods based on pressure correction methods, the discrete system of equations is derived by integrating the governing differential equations over the control volume [1]. For flows with arbitrary geometries, the number of interpolations to obtain flow variables at the cell boundaries for the present grid layout is as small as for any of the grid layouts discussed previously. Enhanced convergence rate is partly attributed to the grid layout which requires

fewer interpolations.

The pressure correction equation for compressible flows is described below. As in the standard pressure correction method [1], the density, the velocities, and the pressure are decomposed as;

$$\rho = \rho^* + \rho' \tag{13}$$

$$u = u^* + u', \tag{14}$$

$$v = v^* + v', \tag{15}$$

$$p = p^* + p' \tag{16}$$

where the superscript * denotes the current values of the flow variables which may not satisfy the conservation of mass equation yet. The discrete momentum equation for u-velocity can be written as;

$$A_p u_p = \sum A_{nb} u_{nb} - \frac{\partial p}{\partial x} + Sv_u \tag{17}$$

where A_p is the coefficient of the u-velocity at the grid point P, Sv_u is the load vector originating from the curvilinear grid structure, and the pressure gradient was left in continuous form deliberately. Substituting eqs. (13-16) into eqs. (17) yields;

$$A_p(u^*_p+u'_p) = \sum A_{nb}(u^*_{nb}+u'_{nb}) - \frac{\partial(p^*+p')}{\partial x} + Sv_u \tag{18}$$

The discrete u-momentum equation based on the current flow variables which may not satisfy the conservation of mass equation can be written as;

$$A_p u^*_p = \sum A_{nb} u^*_{nb} - \frac{\partial p^*}{\partial x} + Sv_u \tag{19}$$

Subtracting eq. (19) from eq. (18) yields;

$$u' = - A_u \frac{\partial p'}{\partial x} \tag{20}$$

where $A_u = 1/A_p$. In deriving eq. (20), the summation over the neighboring grid points and the load vectors in eqs. (18) and (19) have been neglected. The relationship between the incremental v-velocity and the pressure gradient in the y-coordinate direction can be obtained by the same procedure and is given as;

$$v' = - A_v \frac{\partial p'}{\partial y} \tag{21}$$

The incremental pressure is related to the incremental density as;

$$p' = \rho' RT \tag{22}$$

where eq. (22) has been obtained from the equation of state. The conservation of mass equation is given as;

$$\nabla \cdot (\rho \mathbf{V}) = 0$$

or,

$$\nabla \cdot (\rho' \mathbf{V}^*) + \nabla \cdot (\rho^* \mathbf{V}') + \nabla \cdot (\rho' \mathbf{V}') = -\nabla \cdot (\rho^* \mathbf{V}^*) \tag{23}$$

Substituting eqs. (20-22) into (23) yields, after some rearrangement;

$$\frac{\partial}{\partial x}\left[\frac{u^*}{RT}p'\right] + \frac{\partial}{\partial y}\left[\frac{v^*}{RT}p'\right] = \frac{\partial}{\partial x}\left[\rho^* A_u \frac{\partial p'}{\partial x}\right] + \frac{\partial}{\partial y}\left[\rho^* A_v \frac{\partial p'}{\partial y}\right] - \nabla\cdot(\rho^* \mathbf{V}) \qquad (24)$$

where the higher order perturbation term $\nabla\cdot(\rho'\mathbf{V}')$ has been neglected in deriving eq. (24). The last term in eq. (24) represents the mass imbalance. Integrating eq. (24) over a pressure control volume yields;

$$\oint \left\{\frac{u^* n_x + v^* n_y}{RT}p'\right\}ds - \oint \left\{(\rho^* A_u \frac{\partial \xi}{\partial x} n_x + \rho^* A_v \frac{\partial \xi}{\partial y} n_y)\frac{\partial p'}{\partial \xi}\right\}ds$$

$$- \oint \left\{(\rho^* A_u \frac{\partial \eta}{\partial x} n_x + \rho^* A_v \frac{\partial \eta}{\partial y} n_y)\frac{\partial p'}{\partial \eta}\right\}ds = \oint -\nabla\cdot(\rho^* \mathbf{V}^*)dx \qquad (25)$$

where the Green-Gauss theorem has been made use of to invert the volume integration into a surface integration. The discrete control volume equation for eq. (25) can be written as;

$$A_P p'_P = A_E p'_E + A_W p'_W + A_S p'_S + A_N p'_N + Sc_{p'} + Sv_{p'} \qquad (26)$$

where $Sc_{p'}$ is a load vector of the mass imbalance and $Sv_{p'}=-A_\xi \partial p'/\partial\xi + A_\eta \partial p'/\partial\eta$ contains all the contributions made by the curvilinear grid. Note that the variable load vector $Sv_{p'}$ is a null vector in the first sweep. After the first sweep, the $Sv_{p'}$ term was updated in each sweep using the incremental pressure obtained in the previous sweep.

The other flow equations were solved by the same procedure as that of

the pressure correction equation. However, the load vector Sv_i ($i=u,v,t,k,\epsilon$) is not a null vector and was evaluated only once in each iteration. The upwind difference approximation [1] has been used to solve the pressure correction equation; and the power law difference approximation [1], for the other flow equations. The incremental pressure is obtained by solving eq. (26), and the corresponding incremental velocities are obtained from eqs. (20-21). The flow variables are updated by using eqs. (14-16), and these updated flow variables are used in computing the new current flow variables by solving eqs. (2-4) together with the turbulence equations. The discrete finite difference system of equations was solved iteratively using the TDMA until the residuals became smaller than the prescribed convergence criteria. Each iteration consisted of 7 sweeps of the pressure correction equation and 3 sweeps for the rest of the flow equations in the flow direction and in the transverse direction, respectively. The convergence criteria used are;

$$R_1 = \sum_{c=1}^{N_c} |\nabla \cdot \hat{\rho}\hat{V}|_c < e_1 \tag{27}$$

$$R_2 = |(a_{i,j}^{n+1} - a_{i,j}^{n})/A_i^{n+1}| < e_2, \quad j=1,N, \tag{28}$$

where N_c is the number of control volumes for the pressure correction equation; the subscript i=(u, v, p, T, k, ϵ) denotes each flow variable; the subscript j denotes each grid point; N denotes the number of degrees of freedom for each flow variable; and A_i denotes the maximum magnitude of the i-th flow variable. The iteration was terminated when either eq. (27) or eq. (28) was satisfied.

Each flow variable was updated using an under-relaxation factor [1].

The under-relaxation procedure was incorporated into the systems of equations for all flow equations except that of the pressure correction equation. The pressure correction equation was solved without under-relaxation; however, the pressure was obtained by adding the incremental pressure multiplied by an under-relaxation factor. No symptom that might lead to a velocity-pressure decoupled solution was observed in the present method. For incompressible flows, $R=1.0\times10^{15}$ has been used in eq. (24) or in eq. (25). Thus, elimination of the velocity - pressure decoupling mechanism is achieved by the numerical method itself and has nothing to do with the inclusion of the convection term into the pressure correction equation.

COMPUTATIONAL RESULTS

The numerical method described in the previous sections was tested and evaluated by solving a number of flow cases. Example flows presented herein include: a developing laminar channel flow, a developing laminar pipe flow, a lid-driven square cavity flow [19-21], a two-dimensional laminar flow through a 90-degree bent channel, a laminar polar cavity flow [22], and a supersonic flow over a compression ramp with shock wave - turbulent boundary layer interaction [23-24]. It is shown from the first three flow cases that the present method does not yield any velocity-pressure decoupled solution, and in fact, there was no symptom of the velocity-pressure decoupling for any of the flow cases considered. The rest of the flow cases were considered to test the accuracy, the convergence nature, and the applicability of the present method to flow problems of practical importance. Further application of the numerical method as well as the turbulence model to a shock wave - turbulent boundary layer

interaction in a transonic flow over an axisymmetric curved hill [18] can be found in Reference 17.

Developing Laminar Channel Flow

A developing laminar channel flow at Re=25 is considered below. The Reynolds number is based on the inlet velocity and the channel width. The exit boundary was located at seven channel widths downstream of the inlet. Uniform velocity was prescribed at the inlet boundary; and vanishing gradient boundary condition for velocities, at the exit boundary. The flow domain was discretized by an equally spaced mesh as well as by an unequally spaced mesh with 41 grid points in the flow direction and 26 in the transverse direction in each case. The unequally spaced mesh is shown in Figure 2-(a). The convergence criteria used were $e_1=e_2=1.0\times10^{-4}$ and the converged solution was obtained after approximately 410 iterations. The residuals at the time of convergence were $R_1=9.4\times10^{-5}$ and $R_2=1.1\times10^{-4}$. The calculated velocity profile at the exit boundary is compared with the exact solution in Figure 2-(b). It can be seen in the figure that the present method almost yields the exact solution.

Developing Laminar Pipe Flow

A developing laminar pipe flow at Re=25 was solved to test the possible existence of the velocity-pressure decoupling for the axisymmetric flow case. The Reynolds number is based on the inlet velocity and the radius of the pipe. The exit boundary was located at seven radii downstream of the inlet. An equally spaced mesh and an unequally spaced mesh with 41x26 grid points were used as in the previous case. The unequally spaced mesh is shown in Figure 3-(a). The boundary conditions, the initial guess,

and the convergence criteria used are the same as in the previous channel flow case. The converged solution was obtained after approximately 170 iterations and the residuals at the time of convergence were R_1=4.2x10^{-4} and R_2=9.1x10^{-5}. Again, it can be seen in Figure 3-(b) that the present method almost yields the exact solution.

Lid-Driven Square Cavity Flow

A lid-driven cavity flow at Re=1000 is considered below to further confirm that the present numerical method is free of the velocity -pressure decoupling mechanism. As a remark, the computational results obtained by the finite difference methods using fine grids can be found in References 19 and 20 and those obtained by a finite element method can be found in Reference 21. The computational domain was discretized by an unequally spaced 81 X 81 mesh with concentration of the grid points in the near wall region. The boundary conditions and the initial guess used are the same as in Reference 21. The converged solution was obtained after approximately 590 iterations for e_1=e_2=1.0x10^{-4}. The residuals at the time of convergence were R_1=2.0x10^{-4} and R_2=1.0x10^{-4}. The calculated streamline contour is shown in Figure 4. It can be seen in the figure that the secondary vortices in the bottom corners were accurately resolved by the present method.

Two-Dimensional Laminar Flow Through a 90-Degree Bent Channel

A two-dimensional laminar flow through a 90-degree bent channel for Re=1000 is considered below. The Reynolds number is based on the channel width and the bulk velocity. It is shown from this flow case that the present numerical method can solve flows with arbitrary geometries as easily as flows with rectangular geometries. Note that the numerical

methods adopting the fully staggered grid layout and solving for the cartesian velocities can not be used to solve this flow case. The inlet boundary was located at 5 channel widths upstream of the curved section; and the exit boundary, at 15 channel widths downstream of the curved section. The flow domain was discretized by 71 grid points in the flow direction and 25 in the transverse direction. The velocity profile of a fully developed channel flow was prescribed at the inlet boundary. The vanishing gradient boundary condition was used for velocities at the exit boundary. The convergence criteria used were $e_1=e_2=1.0\times10^{-4}$. The converged solution was obtained after approximately 500 iterations. The residuals at the time of convergence were $R_1=8.3\times10^{-2}$ and $R_2=1.0\times10^{-4}$. The mass flow rate, obtained from the prescribed inlet velocity profile, through the inlet boundary was 0.814419 Kg/m-sec and the calculated mass flow rate leaving the exit boundary was 0.814401 Kg/m-sec. Hence the relative mass imbalance was 2.2×10^{-5}. The grids, the calculated streamline contour, and the pressure contour in the vicinity of the curved section for Re=1000 is shown in Figure 5.

Laminar Polar Cavity Flow

A laminar polar cavity flow at Re=60 and 350 is considered below to test the accuracy of the present numerical method. The Reynolds number is based on the azimuthal velocity and the radius of curvature of the lid. The polar cavity is schematically shown in Figure 6. The experimental data can be found in Reference 22. The flow domain was discretized by 81x81 grid points, as in the Reference 22, with concentration of grid points in the corner regions. The Dirichlet boundary condition for velocities was prescribed at all boundaries. The convergence criteria used were

e_1-e_2-4.0×10^{-5}. For Re=60, the converged solution was obtained after approximately 810 iterations and the residuals were R_1-1.5×10^{-3} and R_2-3.9×10^{-5}. For Re=350, the converged solution was obtained after approximately 820 iterations and the residuals at the time of convergence were R_1-7.1×10^{-3} and R_2-3.7×10^{-5}. In each case, the required computational time was approximately 8 minutes for the CRAY/XMP at the NASA/LeRC.

The calculated azimuthal and radial velocity profiles at three azimuthal locations for Re=60 are compared with experimental data as well as the computational results of Reference 22 in Figures 7-(a) and 7-(b), respectively. It can be seen that the present computational results and those obtained using the standard SIMPLE method [22] compare favorably with experimental data. The present method yielded a slightly better radial velocity profile at θ=20 degrees as shown in Figure 7-(b). The calculated streamline, pressure, and the vorticity contours are shown in Figure 8. It can be seen from the pressure contour and the vorticity contour that the potential core has not been well established at Re=60.

The calculated azimuthal and radial velocity profiles at the same three azimuthal locations for Re=350 are compared with experimental data as well as those of Reference 22 in Figure 9. It can be seen in the figure that both computational results are in good agreement with the experimental data. It is mentioned in Reference 22 that the first order differencing method yielded inaccurate computational results for the polar cavity flow at Re=350. However, it can be seen in the figure that the present method yielded as accurate computational results as those obtained using the second order differencing method of Reference 22. It can be seen from the pressure and the vorticity contours that the potential core has been well established at Re=350.

Turbulent Supersonic Flow over a Compression Ramp

A turbulent supersonic flow over a 24-degree compression ramp is considered below. The experimental data can be found in References [23-24]. The free stream Mach number was 2.85, the boundary layer thickness of the approaching supersonic flow was 0.0211 meters, and the Reynolds number based on the free stream condition and the boundary layer thickness was 1.13×10^6.

In the numerical calculation, the inlet boundary was located at 2.17 boundary layer thicknesses upstream of the corner; and the exit boundary, at five boundary layer thicknesses downstream of the corner. The top boundary was located at seven boundary layer thicknesses away from the wall. The flow domain was discretized by 97 grid points in the flow direction and 56 in the transverse direction. The partition between the near-wall layer and the external region was located at approximately 4.5 per cent of the boundary layer thickness away from the wall and 14 grid points were allocated inside the near-wall layer. The grid size in the normal direction was increased by a factor of approximately 1.2. The inlet boundary condition for the tangential velocity and the turbulent kinetic energy were obtained from experimental data for a fully developed flat plate flow [29]. The non-dimensional velocity and the turbulent kinetic energy profiles were scaled to yield a boundary layer thickness of 0.0211 meters at the inlet boundary. Uniform static pressure and uniform enthalpy were also prescribed at the inlet boundary. The no-slip boundary condition for velocities, vanishing turbulent kinetic energy, and a constant temperature which corresponds to the free stream stagnation temperature were prescribed at the solid wall boundary. The free stream flow condition

was prescribed at the top boundary, and the vanishing gradient boundary condition was used for all flow variables at the exit boundary. The initial guess was obtained by extending the inlet boundary condition in the flow direction. The converged solution was obtained after approximately 1400 iterations for $e_1=e_2=4.0\times10^{-4}$. At the time of convergence R_1 and R_2 were 3.5×10^{-4} and 4.0×10^{-4}, respectively. The mass flow rate through the inlet boundary, obtained from the prescribed inlet boundary conditions, was 68.434 Kg/m-sec and the calculated mass flow rate leaving the exit boundary was 68.411 Kg/m-sec. Hence the relative mass imbalance was 3.4×10^{-4}. The required computational time was approximately 18 minutes for the CRAY/XMP at the NASA/LeRC.

The calculated static pressure on the wall is compared with experimental data as well as the computational result obtained using a relaxation turbulence model [24] in Figure 11. In Reference 24, several sets of computational results obtained using various turbulence models were presented. The wall pressure obtained using a relaxation turbulence model [24] compared most favorably with the experimental data. It can be seen in the figure that the present turbulence model yielded slightly compressed pressure distribution. The level of agreement between the experimental data and all the other computational results of Reference 24 was almost the same as that of the present computational result.

The mean velocity profiles at $s/\delta=-2.17$, 0.0, and 2.89 are compared with experimental data as well as with those obtained using the relaxation turbulence model [24] in Figure 12, where the distance (s) has been measured from the corner along the surface and δ is the boundary layer thickness. It can be seen that the present computational results compare more favorably with the experimental data than does the other computational

result [24]. The level of agreement between the best computational result in Reference 24 and the experimental data was almost the same as that of the present case. Note that the velocity profiles obtained using the relaxation model compared less favorably with the experimental data than those obtained using the other turbulence models [24].

The calculated streamline contour is shown in Figure 13-(a). The measured flow separation zone extended from $s/\delta \approx -1.44$ to $s/\delta \approx 0.5$. The present method yielded the flow recirculation zone extending from $s/\delta = -0.72$ to $s/\delta = 0.68$. The levels of agreement between the measured flow recirculation zone and all the computational results, including the present result, were almost the same. However, the relaxation model which yielded the best wall pressure yielded the worst flow recirculation zone. The calculated static pressure contour lines are shown in Figure 13-(b), where the pressure has been normalized by the inlet total pressure and the incremental pressure between the contour lines is 0.2. The calculated iso-Mach lines and the turbulent kinetic energy contours are shown in Figures 13-(c) and 13-(d), respectively. The incremental Mach number between the iso-Mach lines is 0.2 in Figure 13-(c). It has been shown in this example that the present computational result compared as favorably with the experimental data as any other computational results [24].

CONCLUSIONS

A control-volume based finite difference method to solve the Reynolds averaged Navier-Stokes equations for all flow velocities has been presented.

It has been shown from the developing channel flow, the developing pipe flow, and the lid-driven square cavity flow that the present numerical

method is free of the velocity-pressure decoupling. For the channel and the pipe flows, the method almost yields the exact solutions. For the polar cavity flow, the present method yielded as accurate computational results as the second order differencing method [22]. The turbulent supersonic flow over the 24-degree compression ramp [23-24] was solved using a k-ϵ turbulence model supplemented with a near-wall turbulence model. In the method, the dissipation rate inside the near-wall region was obtained from an algebraic equation and that for the rest of the flow domain was obtained by solving the differential equation for the dissipation rate. This approach was found to be more advantageous than the low Reynolds number turbulence models since the stiff dissipation rate equation in the near-wall region need not be solved numerically. The computational results for the supersonic compression corner flow compared as favorably with the experimental data as any other computational results [24].

It has also been shown that the present numerical method yields accurate computational results even when highly skewed, unequally spaced, curved grids were used. Equally importantly, the present method was found to be strongly convergent for high Reynolds number flows as well as for flows with complex geometries. This strongly convergent nature is attributed, in part, to the use of the pressure staggered grid layout.

REFERENCES

1. Patankar, S.V.: Numerical Heat Transfer and Fluid Flow. McGraw-Hill, New York, 1980.

2. Gosman, A.D.; and Ideriah, F.J.K.: TEACH-T, Department of Mechanical Engineering, Imperial College, London, 1982.

3. Kline, S.J.; Cantwell, B.J.; and Lilley, G.M. eds.: Complex Turbulent Flows, Vols. 1-3, Mechanical Engineering Dept., Stanford University, 1981.

4. Jones, W.P.; and Whitelaw, J.H.: Calculation Methods for Reacting Turbulent Flows: A Review." Combust. Flame, vol. 48, no. 1, Oct. 1982, pp. 1-26.

5. Beam, R.M.; and Warming, R.F.: An Implicit Factored Scheme for the Compressible Navier-Stokes Equations. AIAA J., vol. 16, no. 4, Apr. 1978, pp. 393-402,

6. MacCormack, R.W.: A Numerical Method for Solving the Equations of Compressible Viscous Flow. AIAA J., vol. 20, no. 9, Apr. 1982, pp. 1275-1281.

7. Shyy, W.; Tong, S.S.; and Correa, S.M.: Numerical Recirculating Flow Calculation Using a Body-Fitted Coordinate System. Numerical Heat Transfer, vol. 8, no. 1, 1985, pp. 99-113.

8. Maliska, C.R.; and Raithby, G.D.: A Method for Computing Three Dimensional Flows Using Non-Orthogonal Boundary-Fitted Coordinates. Int. J. Numer. Methods Fluids, vol. 4, no. 6, June 1984, pp. 519-537.

9. Rhie, C.M.: A Pressure Based Navier-Stokes Solver Using the Multigrid Method. AIAA Paper 86-0207, Jan. 1986.

10 Dwyer; H.A.; and Ibrani, S.: Time Accurate Solutions of the Incompressible and Three-Dimensional Navier-Stokes Equations. AIAA Paper 88-0418, Jan. 1988.

11. Karki, K.C.; and Patankar, S.V.: A Pressure Based Calculation Procedure for Viscous Flows at All Speeds in Arbitrary Configurations. AIAA Paper 88-0058, Jan. 1988.

12. Vanka; S.P.; Chen, B.C.J.; and Sha, W.T.: A Semi-Implicit Calculation Procedure for Flows Described in Boundary-Fitted Coordinate Systems. Numerical Heat Transfer, vol. 3, no. 1, 1980, pp. 1-19.

13. Chen, Y.S.: Viscous Flow Computations Using a Second-Order Upwind Differencing Scheme. AIAA Paper 88-0417, Jan. 1988.

14. Fortin, M.; and Fortin, A.: Newer and Newer Elements for Incompressible Flow. Finite Elements in Fluids, vol. 6, R.H. Gallagher, et al., eds., J. Wiley and Sons, New York, 1985, pp. 171-187.

15. Raithby, G.D.; and Schneider, G.E.: Numerical Solution of Problems in Incompressible Fluid Flow: Treatment of the Velocity-Pressure Coupling. Numerical Heat Transfer, vol. 2, no. 4, 1979, pp. 417-440.

16. Kim, S.W.: A Near-Wall Turbulence Model and Its Application to Fully Developed Turbulent Channel and Pipe Flows. NASA TM-101399, 1988.

17. Kim, S.W.: Numerical Computation of Shock Wave - Turbulent Boundary Layer Interaction in Transonic Flow Over an Axisymmetric Curved Hill. NASA TM-101473, 1989.

18. Johnson, D.A.; Horstman, C.C.; and Bachalo, W.D.: Comparison Between Experiment and Prediction for a Transonic Turbulent Separated Flow. AIAA J., vol. 20, no. 6, June 1982, pp. 737-744.

19. Ghia, U.; Ghia, K.N.; and Shin, C.T.: High-Re Solutions for Incompressible Flow Using the Navier-Stokes Equations and a Multigrid Method. J. Comput. Phys., vol. 48, no. 3, Dec. 1982, pp. 387-411.

20. Schreiber, R.; and Keller, H.B.: Driven Cavity Flows by Efficient Numerical Techniques. J. Comput Phys., vol. 49, no. 2, Feb. 1983, pp. 310-333.

21. Kim, S.W.: A Fine Grid Finite Element Computation of Two-Dimensional High Reynolds Number Flows. Computers Fluids, vol. 16, no. 4, 1988, pp. 429-444.

22. Fuchs, L.; and Tillmark, N.: Numerical and Experimental Study of Driven Flow in a Polar Cavity. Int. J. Numer. Methods Fluids, vol. 5, no. 4, Apr. 1985, pp. 311-329.

23. Settles, G.S.; Vas, I.E.; and Bogdonoff, S.M.: Details of a Shock-Separated Turbulent Boundary Layer at a Compression Corner. AIAA J., vol. 14, no. 12, Dec. 1976, pp. 1709-1715.

24. Horstman, C.C., et al.: Reynolds Number Effects on Shock-Wave Turbulent-Boundary Layer Interactions. AIAA J., vol. 15, no. 8, Aug. 1977, pp. 1152-1158.

25. White, F.M.: Viscous Fluid Flow. McGraw-Hill, New York, 1974.

26. Harlow, F.H.; and Nakayama, P.I.: Transport of Turbulence Energy Decay Rate. LA-3854, Los Alamos Scientific Lab, 1968.

27 Kim, S.W.; and Chen, Y.S.: A Finite Element Computation of Turbulent Boundary Layer Flows with an Algebraic Stress Turbulence Model. Comput. Methods Appl. Mech. Eng., vol. 66, no. 1, 1988, pp. 45-63.

28 Kim, S.W.; and Chen, C.P.: A Multiple-Time-Scale Turbulence Model Based on Variable Partitioning of the Turbulent Kinetic Energy Spectrum. To appear in Numerical Heat Transfer, 1989. (Also available as NASA CR-179222, 1987; and AIAA Paper 88-0221, 1988).

29. Klebanoff, P.S.: Characteristics of Turbulence in a Boundary Layer with Zero Pressure Gradient. NACA Report 1247, 1955.

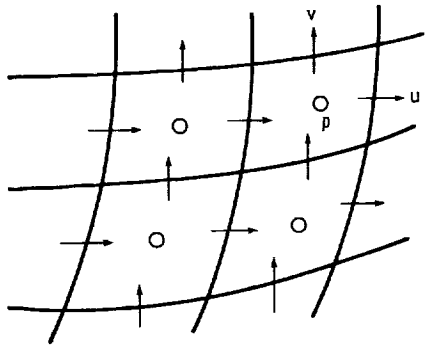

(a) FULLY STAGGERED GRID.

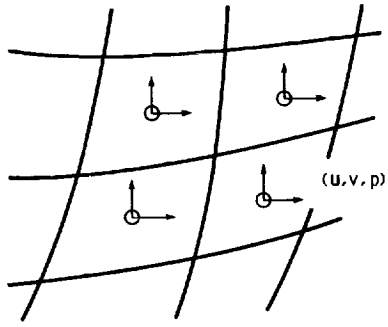

(b) COLLOCATED GRID.

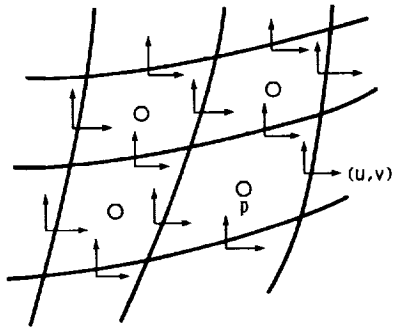

(c) EXTENDED FULLY STAGGERED GRID.

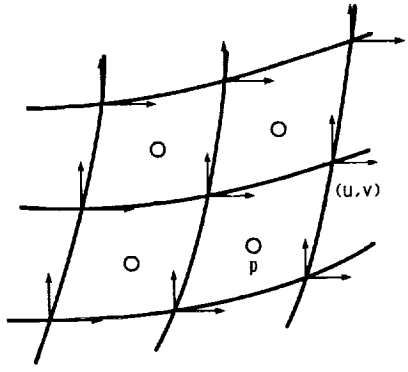

(d) PRESSURE STAGGERED GRID.

FIGURE 1. - GRID LAYOUTS.

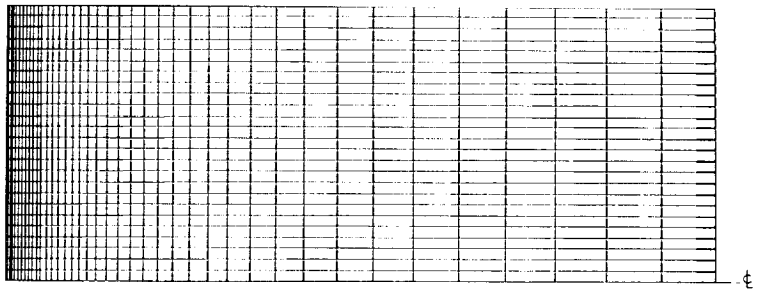

(a) 41 x 26 GRID.

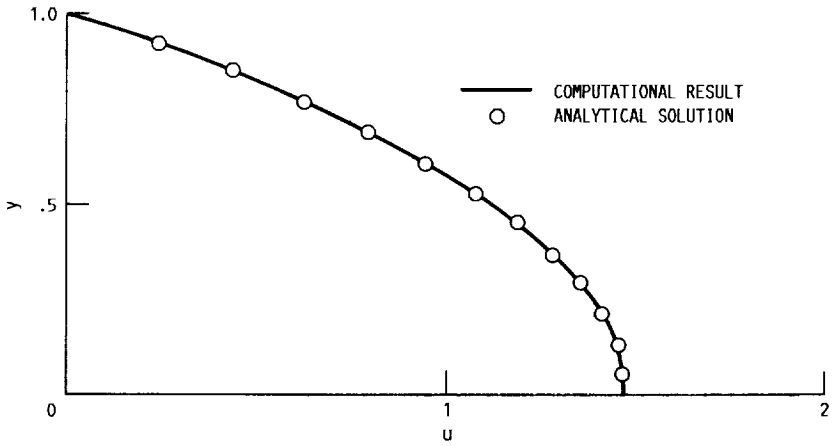

(b) VELOCITY PROFILE.

FIGURE 2. - DEVELOPING LAMINAR CHANNEL FLOW.

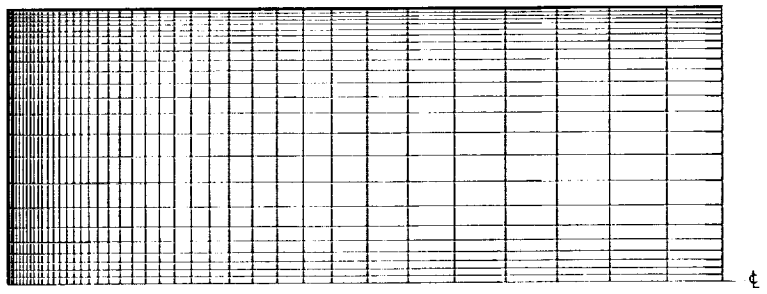

(a) 41 x 26 GRID.

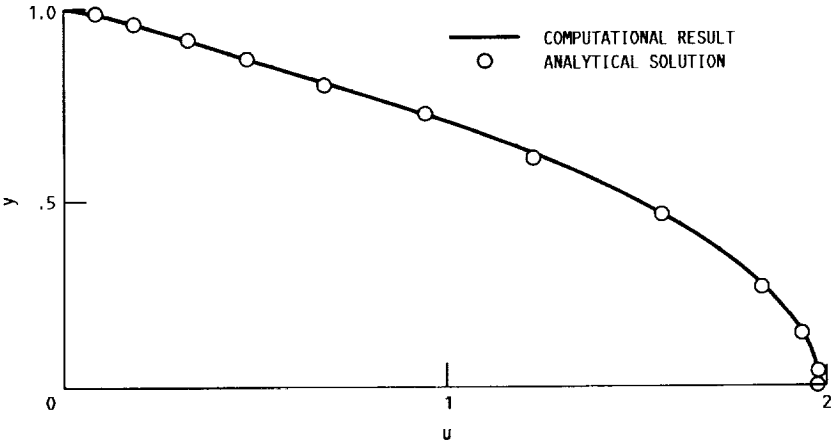

(b) VELOCITY PROFILE.

FIGURE 3. - DEVELOPING LAMINAR PIPE FLOW.

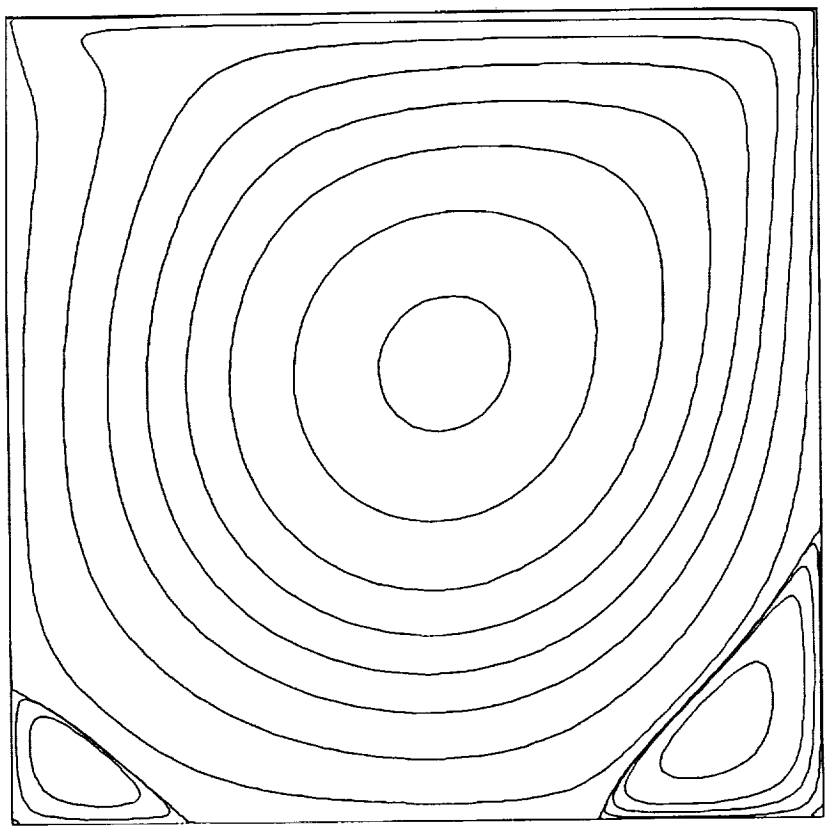

FIGURE 4. - STREAMLINE CONTOUR FOR LID-DRIVEN CAVITY FLOW AT Re = 1000.

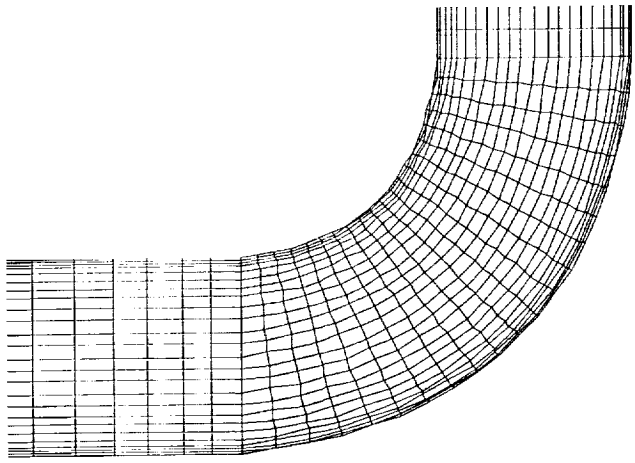

(a) GRID.

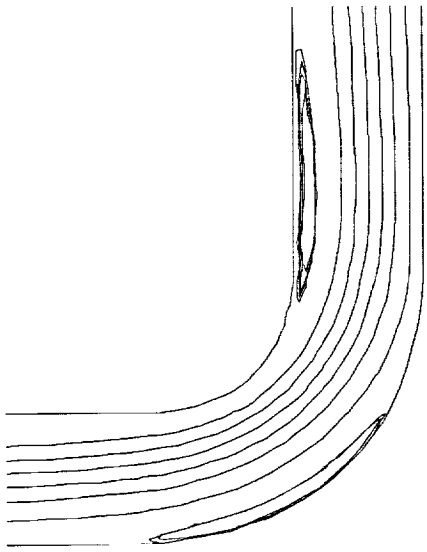

(b) STREAMLINE CONTOUR.

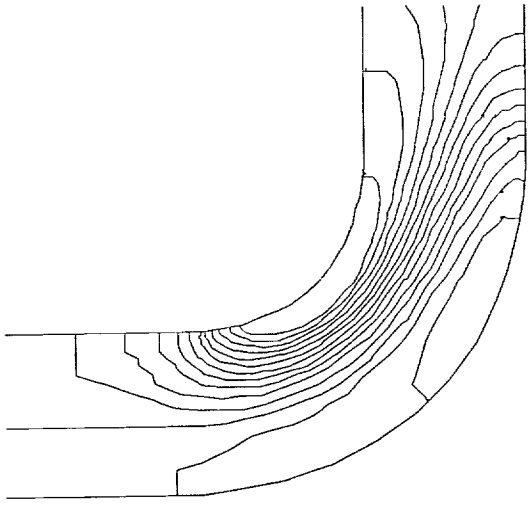

(c) PRESSURE CONTOUR.

FIGURE 5. - LAMINAR FLOW THROUGH A 90-DEGREE BENT CHANNEL.

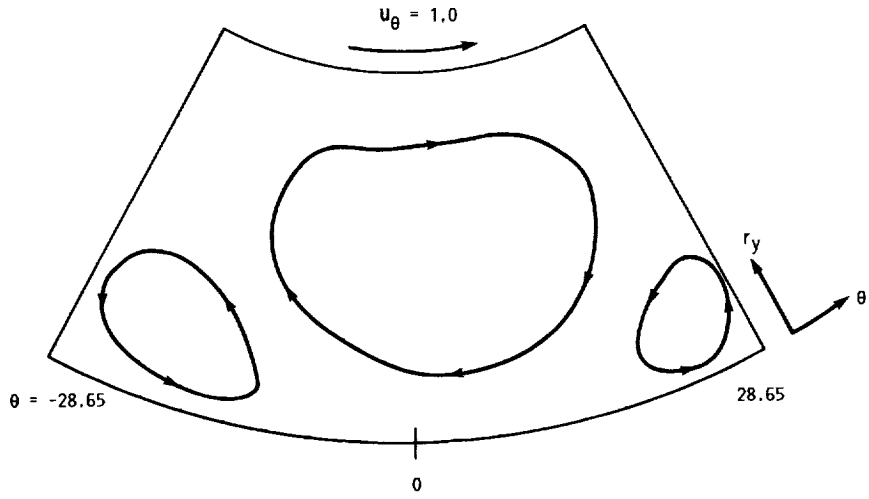

FIGURE 6. - POLAR CAVITY FLOW.

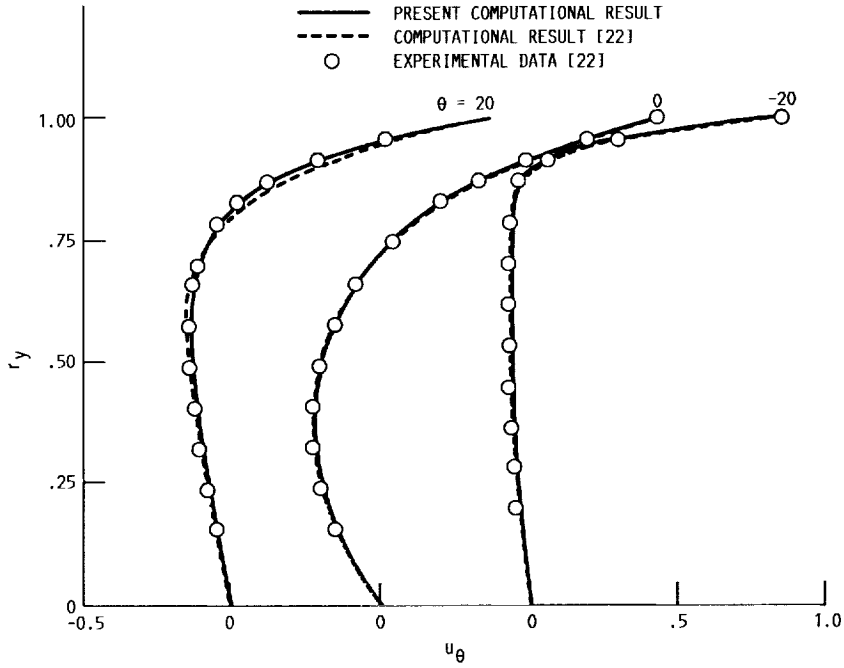

(a) AZIMUTHAL VELOCITY.

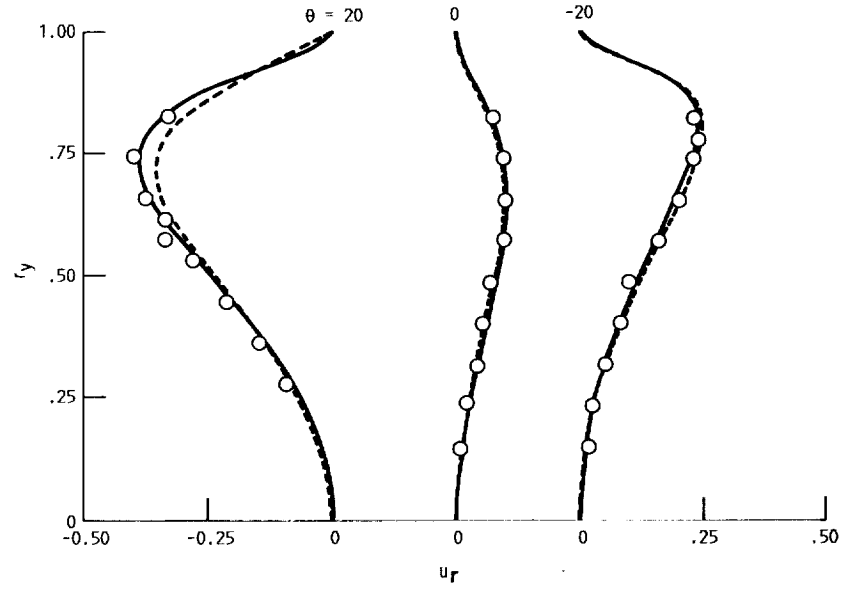

(b) RADIAL VELOCITY PROFILE.

FIGURE 7. - POLAR CAVITY FLOW FOR Re = 60.

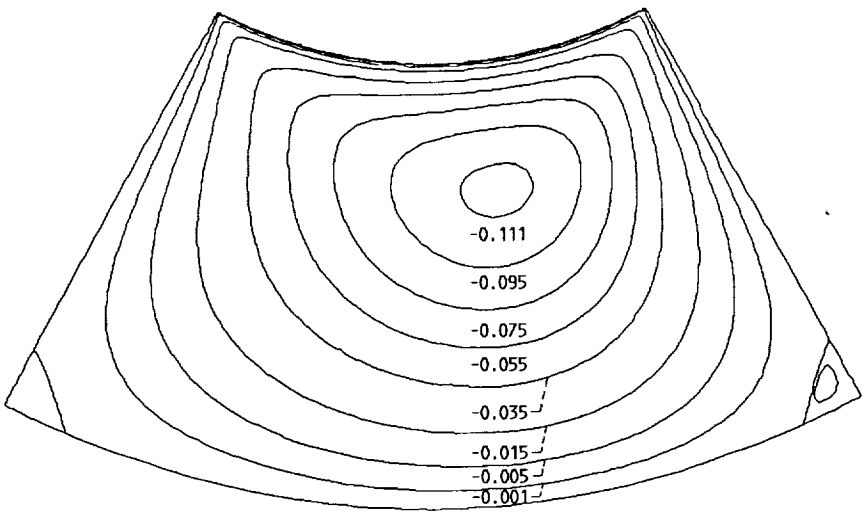

(a) STREAMLINE CONTOUR.

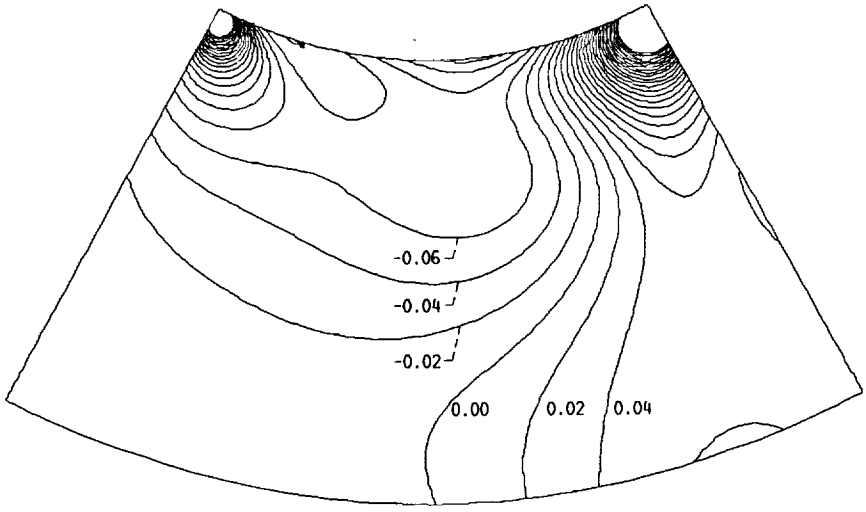

(b) PRESSURE CONTOUR.

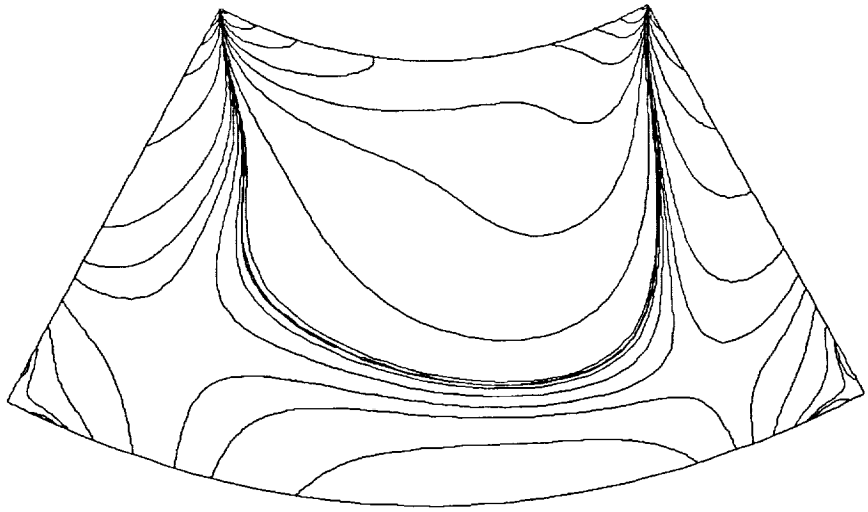

(c) VORTICITY CONTOUR.

FIGURE 8. - POLAR CAVITY FLOW FOR Re = 60.

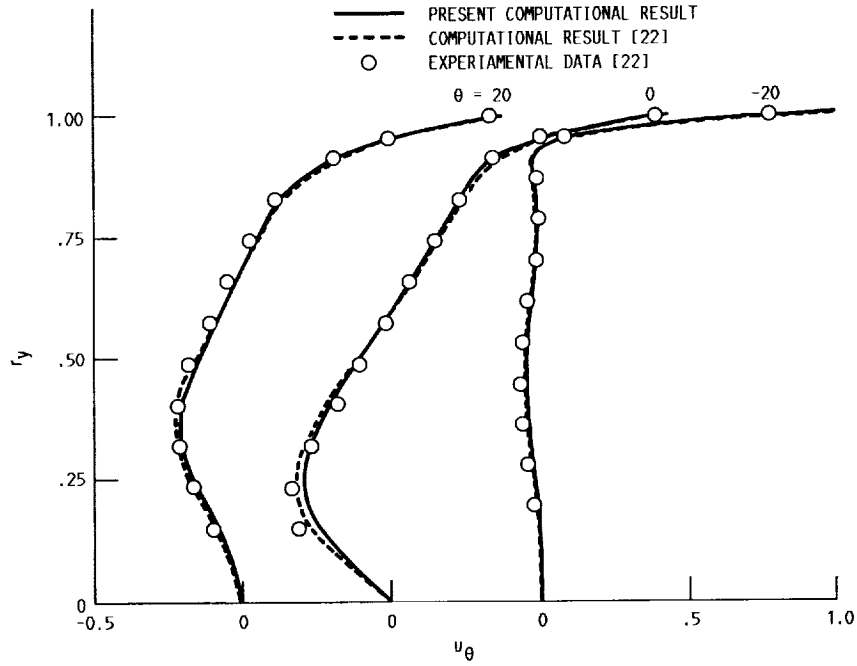

(a) AZIMUTHAL VELOCITY.

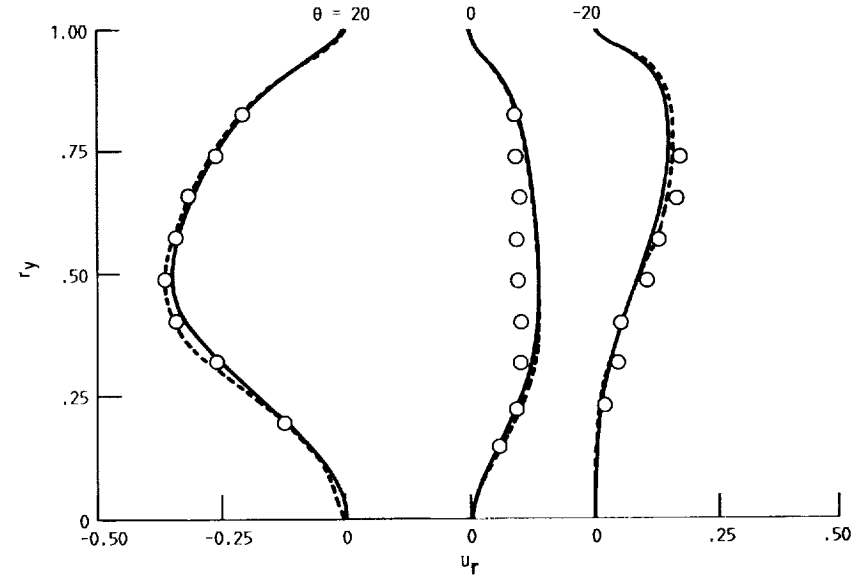

(b) RADIAL VELOCITY PROFILE.

FIGURE 9. - POLAR CAVITY FLOW FOR Re = 350.

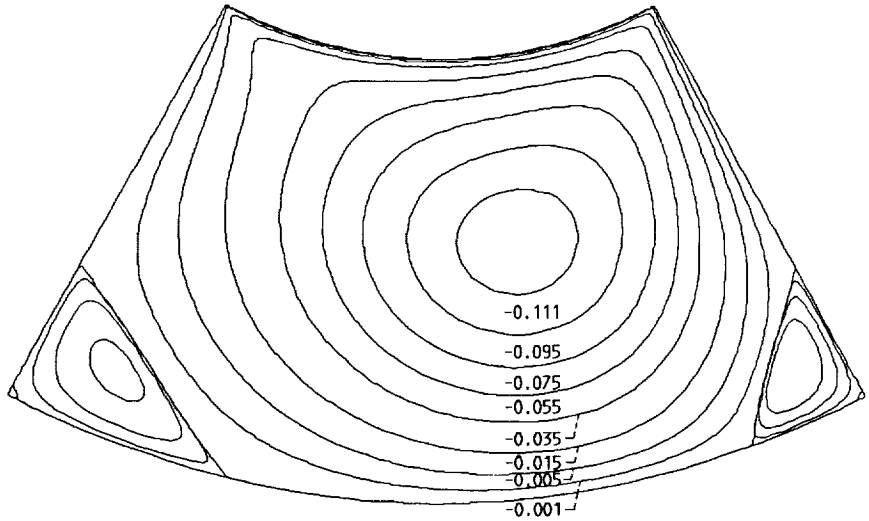

(a) STREAMLINE CONTOUR.

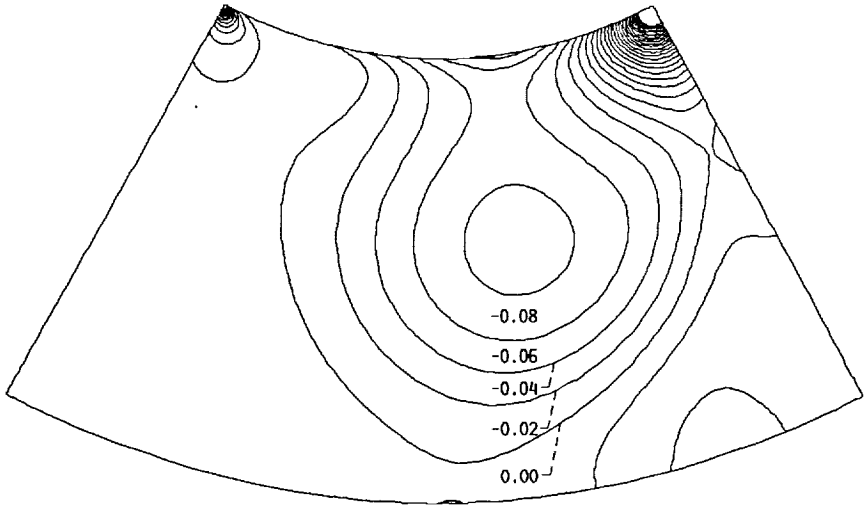

(b) PRESSURE CONTOUR.

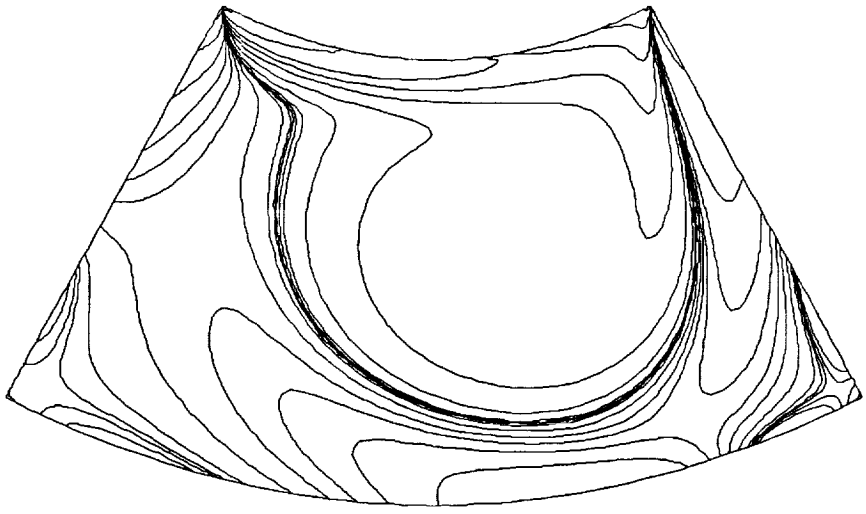

(c) VORTICITY CONTOUR.

FIGURE 10. - POLAR CAVITY FLOW FOR Re = 350.

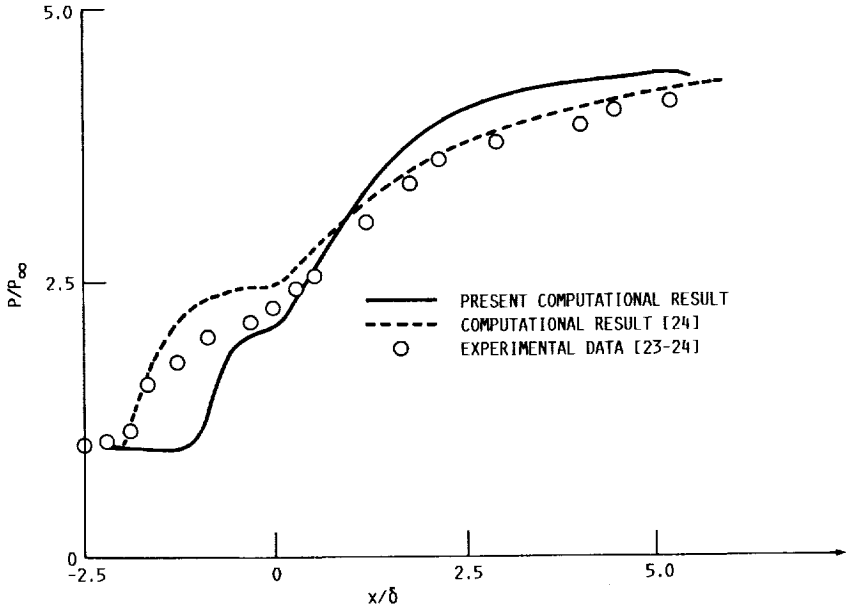

FIGURE 11. - STATIC WALL PRESSURE FOR COMPRESSION CORNER FLOW.

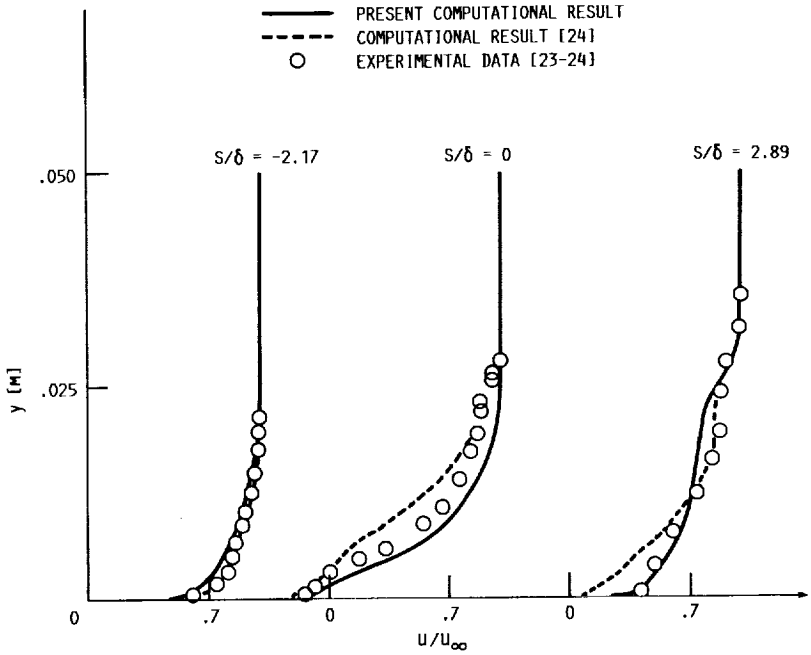

FIGURE 12. - VELOCITY PROFILES FOR COMPRESSION CORNER FLOW.

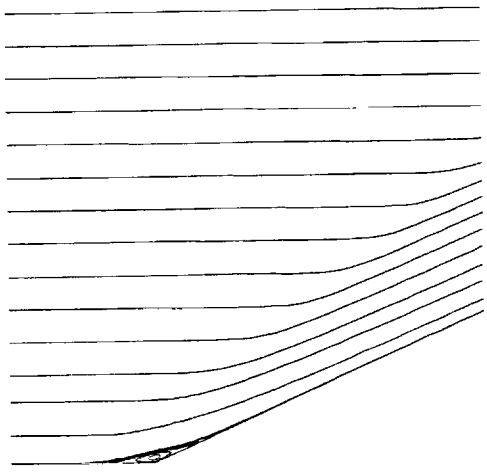

(a) STREAMLINE CONTOUR.

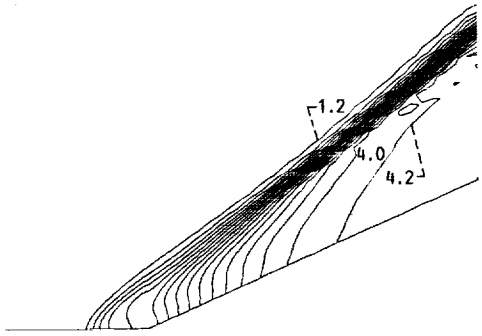

(b) PRESSURE CONTOUR.

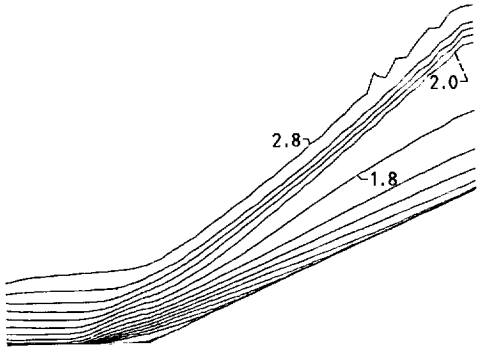

(c) ISO-MACH LINES.

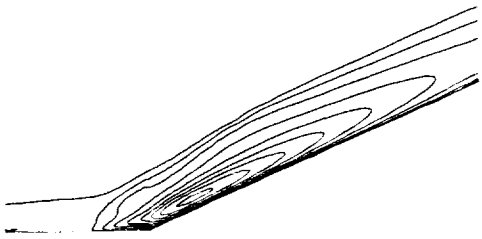

(d) TURBULENT KINETIC ENERGY CONTOUR.

FIGURE 13. - COMPRESSION CORNER FLOW.

NASA
National Aeronautics and Space Administration

Report Documentation Page

1. Report No.	2. Government Accession No.	3. Recipient's Catalog No.
NASA TM-101488 ICOMP-89-5		

4. Title and Subtitle	5. Report Date
Control-Volume Based Navier-Stokes Equation Solver Valid at All Flow Velocities	February 1989
	6. Performing Organization Code
7. Author(s)	8. Performing Organization Report No.
S.-W. Kim	E-4629
	10. Work Unit No.
	505-62-21
9. Performing Organization Name and Address	11. Contract or Grant No.
National Aeronautics and Space Administration Lewis Research Center Cleveland, Ohio 44135-3191	
	13. Type of Report and Period Covered
12. Sponsoring Agency Name and Address	Technical Memorandum
National Aeronautics and Space Administration Washington, D.C. 20546-0001	14. Sponsoring Agency Code

15. Supplementary Notes

S.-W. Kim, Institute for Computational Mechanics in Propulsion, NASA Lewis Research Center (work funded under Space Act Agreement C99066G).

16. Abstract

A control-volume based finite difference method to solve the Reynolds averaged Navier-Stokes equations is presented. A pressure correction equation valid at all flow velocities and a pressure staggered grid layout are used in the method. Example problems presented herein include: a developing laminar channel flow, developing laminar pipe flow, a lid-driven square cavity flow, a laminar flow through a 90-degree bent channel, a laminar polar cavity flow, and a turbulent supersonic flow over a compression ramp. A k-ϵ turbulence model supplemented with a near-wall turbulence model was used to solve the turbulent flow. It is shown that the method yields accurate computational results even when highly skewed, unequally spaced, curved grids are used. It is also shown that the method is strongly convergent for high Reynolds number flows.

17. Key Words (Suggested by Author(s))	18. Distribution Statement
Control volume method Near wall turbulence model polar cavity flow Turbulent flow over compression range	Unclassified – Unlimited Subject Category 34

19. Security Classif. (of this report)	20. Security Classif. (of this page)	21. No of pages	22. Price*
Unclassified	Unclassified	40	A03

*For sale by the National Technical Information Service, Springfield, Virginia 22161